 doi:10.20944/preprints201901.0098.v1

Pilot Feedback Electronic Imaging at Elevated Temperatures and its Potential for In-Process Electron Beam Melting Monitoring

Authors: Hay Wong[a], Derek Neary[a], Eric Jones, Peter Fox[a], Chris Sutcliffe[a]

[a]School of Engineering, University of Liverpool, The Quadrangle, Brownlow Hill, United Kingdom L69 3GH

Corresponding author's email: Hay Wong – hay.wong@liv.ac.uk

Keywords: Additive Manufacturing; Electron Beam Melting; In-Process Monitoring; Quality Control; Electronic Imaging

Abstract

Electron Beam Melting (EBM) is an increasingly used Additive Manufacturing (AM) technique employed by many industrial sectors, including the medical device and aerospace industries. The application of this technology is, however, challenged by the lack of process monitoring and control system that underpins process repeatability and part quality reproducibility. An electronic imaging system prototype has been developed to serve as an EBM monitoring technique, the capabilities of which have been verified at room temperature and at 320$\pm$10°C. Nevertheless, in order to fully assess the applicability of this technique, the image quality needs to be investigated at a range of elevated temperatures to fully understand the influence of thermal noise due to heat. In this paper, electronic imaging pilot trials at elevated temperatures, ranging from room temperature to $650°C$, were carried out. Image quality measure Q of the digital electron images was evaluated, and the influence of temperature was investigated. In this study, raw electronic images generated at higher temperatures had greater Q values, i.e. better global image quality. It has been demonstrated that, for temperatures between $30°C - 650°C$, the influence of temperature on electronic image quality was not adversely affecting the visual clarity of image features. It is envisaged that the prototype has significant potential to contribute to in-process EBM monitoring in many manufacturing sectors.

 doi:10.20944/preprints201901.0098.v1

1. Introduction

Electron Beam Melting (EBM) is an Additive Manufacturing (AM) technique that makes use of an accelerated electron beam to melt metallic powder on a layer-by-layer basis, forming components based on the geometries of the imported three dimensional Computer Aided Design (CAD) models [1]. The ability of the EBM process to form components from metallic powder arises from electron interactions with metallic materials. When an electron beam is accelerated by an anode, focused onto a powder bed by an electromagnetic focusing coil and subsequently deflected to specific locations by an electromagnetic deflection coil, the electrons penetrate the powder particles, whereupon they slow down and convert their kinetic energy into thermal energy. If the energy input is sufficient, the temperature of the powder particles rises above their melting point and sold-to-liquid phase transformation is initiated. When the beam is raster-scanned across the preheated powder bed in a tightly controlled, predefined pattern, melt tracks are solidified to form fully dense cross sections of the desired components. This process is repeated with the additional requirement that the underlying solid is also partially melting to ensure adequate bonding between the underlying and newly formed layers ensuring that full density is achieved.

It is thought that the technique shows great promise in the manufacture of orthopaedic implants and aerospace components. In an evaluation study on powder-based EBM technology, it was concluded that the EBM process would have the flexibility to enable the manufacture of a wide range of complex and difficult-to-fabricate aerospace and biomedical components [2]. The increased design freedom of the EBM process enables the economic manufacture of porous bone ingrowth surfaces for orthopaedic implants [3] while the reduced thermal residual stress and the high-vacuum process environment is beneficial for the production of aircraft components [4]. Nevertheless, both of these industries are highly regulated and their standard manufacturing processes are well established [5, 6]. It is thought that despite the perceived benefits of the EBM process, the transition from the current standard manufacturing techniques to a layered manufacturing approach would not be possible unless a rigorous EBM process monitoring and validation system was available for real-time control [7].

Academic research communities have built different monitoring systems to assess the quality of the EBM process. These system involve the use of infrared (IR) (wavelength between $700nm$ and $1mm$), visible light (wavelength between $400nm$ and $700nm$), X-ray (wavelength between $0.01nm$ and $10nm$) and feedback electrons, i.e. Secondary Electrons (SE) and Backscattered Electrons (BSE). Table 1 summarises the monitoring systems developed.

Table 1 Thermal and optical monitoring system developed for the EBM process

Process Attribute Monitored	Monitoring Method	Process Artefacts	Sensor	Reference
Processing area surface temperature	Thermal imaging	IR	Microbolometer	[8 – 11]
Melt pool geometry	Thermal / optical imaging	IR / visible light	Microbolometer / CMOS sensor	[12 –14]
Processing area topography	Thermal imaging / electronic imaging	IR / electrons	Microbolometer / electrically conductive surface	[15 - 22]

When compared to thermal and optical imaging, it has been shown that electronic imaging has the potential to offer superior flexibility on image Field of View (FOV) and image magnification [21]. Although the electronic image quality has been verified at room temperature and 320°C [22], the image quality is still yet to be evaluated at a full range of elevated temperatures (room to in-process EBM monitoring temperature) to understand the influence of thermal noise due to heat. Noise is defined as the disturbance which obscures a desired signal. Thermal noise arises from the random motion of electrons in any conductor due to temperature effects [23]. The applicability of electronic imaging in EBM monitoring cannot be fully explored without extending the investigation into the influence of thermal noise on image quality when higher temperatures are used.

It is proposed that electronic imaging trials should be carried out at a range of temperatures increasing in value towards the actual in-process monitoring temperature of a demonstrator material. Ti-6Al-4V alloy was chosen to be the demonstrator material for this study due to its popularity in the field of AM, aerospace and medical industries [24, 25].

2. Materials and Methods

2.1 Challenges in Eleveted Temperatures Imaging and Prototype Modification

A bespoke digital electronic imaging system prototype was interfaced with an Arcam A1 EBM machine (GE Additive, USA), hereafter referred to as the EBM machine, to carry out imaging trials at elevated temperatures, as depicted in Fig. 1(a) and (b). The prototype consisted of an electron sensor, a data logger, signal amplifier and image generation software and was designed to generate digital electronic images from the Seconary Electrons (SE) and Backscattered Electrons (BSE), originating from the interactions between the machine's primary electron beam and the processing area [22].

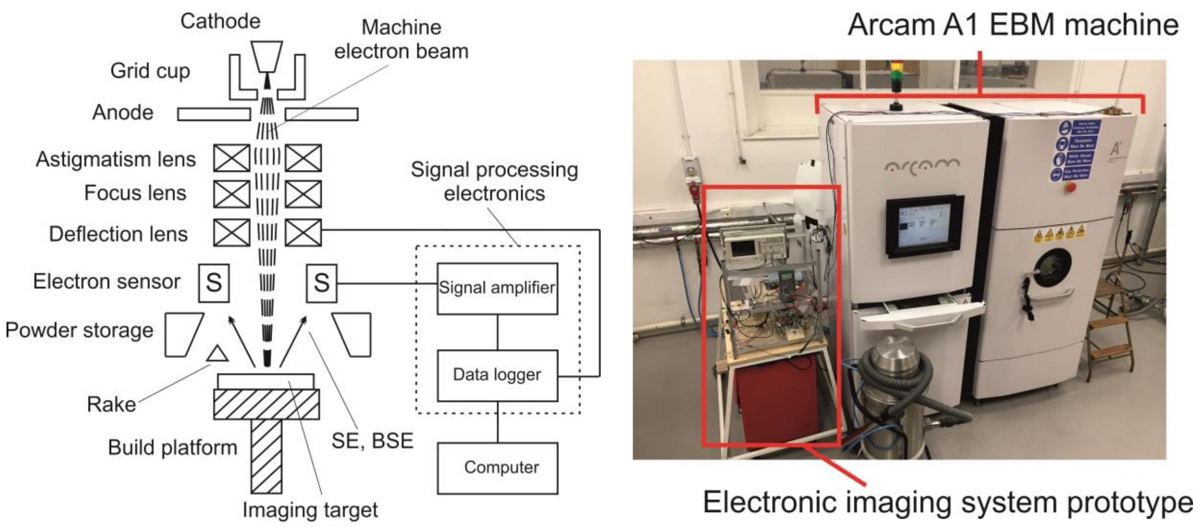

(a) Adapted schematic [21] (b) Laboratory installation

Fig. 1 Electronic imaging system prototype interfaced with an EBM machine

 doi:10.20944/preprints201901.0098.v1

Carrying out image generation at higher temperature is thought to introduce at least two poential challenges: firstly, the yeild of SE and BSE might vary with temperature, and secondly, the signal amplifier (illustrated in Fig, 1(a)) would be required to suppress the SE and BSE signals during the electron beam heating stage. In EBM, different metals are processed using different process parameters. In this study, Ti-6Al-4V alloy was chosen as the demonstrator matieral, and throughout the course of experimentation, the powder bed on the processing area was maintained at approximately $700°C$ achieved by electron beam heating [26].

With regard to the first challenge, the key factor is to determine the influence of temperature on SE and BSE yields. Literature shows that temperature has little to no effect on the yield of SE due to the scale factor of the kinetic energy of an atom, kT (where k is the Boltzmann's constant), which is small when comapred to the averge SE or BSE energy [27]. In general, the average energy of a SE is $2-5eV$. By convention, the minimum energy of a BSE is $50eV$ [28] and the primary electron in an EBM machine has an energy of $60keV$ [29]. At $700°C$, kT has a value of approximately $0.084\ eV$, only 5% of the least energetic SE. As SE and BSE are generated from interactions between a primary electron beam and its target atoms [30], at $700°C$, thermal vibration (proportional to the kinetic energy, kT) of atoms in the target was not expected to affect the combined yield of both SE and BSE, as defined in Eq. 1. This challenge regarding SE and BSE yield at elevated temperatures is thought to be insignificant to this study.

$$\gamma_{SE,BSE} = \frac{I_{SE} + I_{BSE}}{I_{PE}}$$

$$\gamma_{SE,BSE} = \frac{I_T}{I_{PE}} \tag{1}$$

Where

$\gamma_{SE,BSE}$ is the combined SE and BSE yield, I_{SE} (A) and I_{BSE} (A) are the SE and BSE generated from interactions between a primary beam and the imaging target, I_T (A) is the total raw SE and BSE current signal, and I_{PE} (A) is the primary beam current firing at the imaging target.

Regarding the second challenge, the key factor is to suppress input signals to the prototype data logger. The input signal needs to be less than $3V$ due to the choice of data logger, and the signal level should be suppressed when imaging is not taking place. The signal amplifier in the system protoype processes the SE and BSE signals, in the form of electric current, before feeding it into the data logger, as depicted in Fig. 1(a). Eq. 2 defines how the raw electron signal is converted to a voltage and amplified.

$$V_{amp} = G \times R \times I_T$$

$$V_{amp} = A \times I_T \tag{2}$$

Where

V_{amp} (V) is the amplified voltage signal fed into the data logger, G is the gain of the signal amplifier, R (Ω) is the resistance used to convert the electrical current to a voltage in the signal amplifier, I_T (A) is the total raw current signal generated from interactions between the primary electron beam and its target, and A (Ω) is the product of G and R and is defined as the amplification factor

The need for signal suppression arises from the passive nature of the electron sensor. The sensor captures and send signals to the data logger at all times, during both the heating and imaging stages. The primary beam current I_{PE} value assigned for the two stages were different and thus it is expected that the total SE and BSE signals I_T, hereafter referred to as the feedback signal, would be different, even with a constant combined feedback electron yield $\gamma_{SE,BSE}$. The feedback signal should be suppressed during heating and amplified during imaging. In order to handle the feedback signal correctly, modification to the signal amplifier was carried out by introducing two indepentent gain options for the two stages respectively. Table 2 summarises the modified amplifier settings for the two stages and Fig. 2 is a block diagram illustrating the modified signal amplifier.

Table 2 Electronic imaging system prototype signal amplifier settings during heating and imaging. Values rounded to 2 s.f.

Signal Amplifier Parameter	Value (Heating)	Value (Imaging)
Primary electron beam current I_{PE} (mA)	48	1.0
Estimated feedback electron yield $\gamma_{SE,BSE}$	0.3	0.3
Estimated raw feedback signal I_T (mA)	14	0.3
Amplifier amplification factor A	1.1	10,000
Estimated amplifier output V_{amp} (V)	0.016	3.0

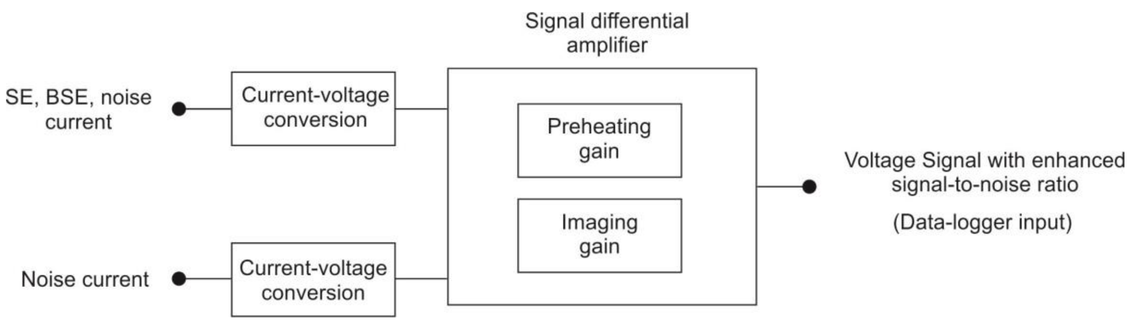

Fig. 2 Modified signal differential amplifier

2.2 Controlled Heating Algorithm Development and Verification Trial

A custom heating algorithm was developed to achieve controlled heating with the use of the EBM machine electron beam. When in use, the beam would be directed to raster scan a heating target to increase the temperature uniformly from room temperature to 700°C, for a typical Ti-6Al-4V build. Fig. 3(a) describes the working principle of the heating algorithm while Fig. 3(b) depicts typical sets of scan lines generated.

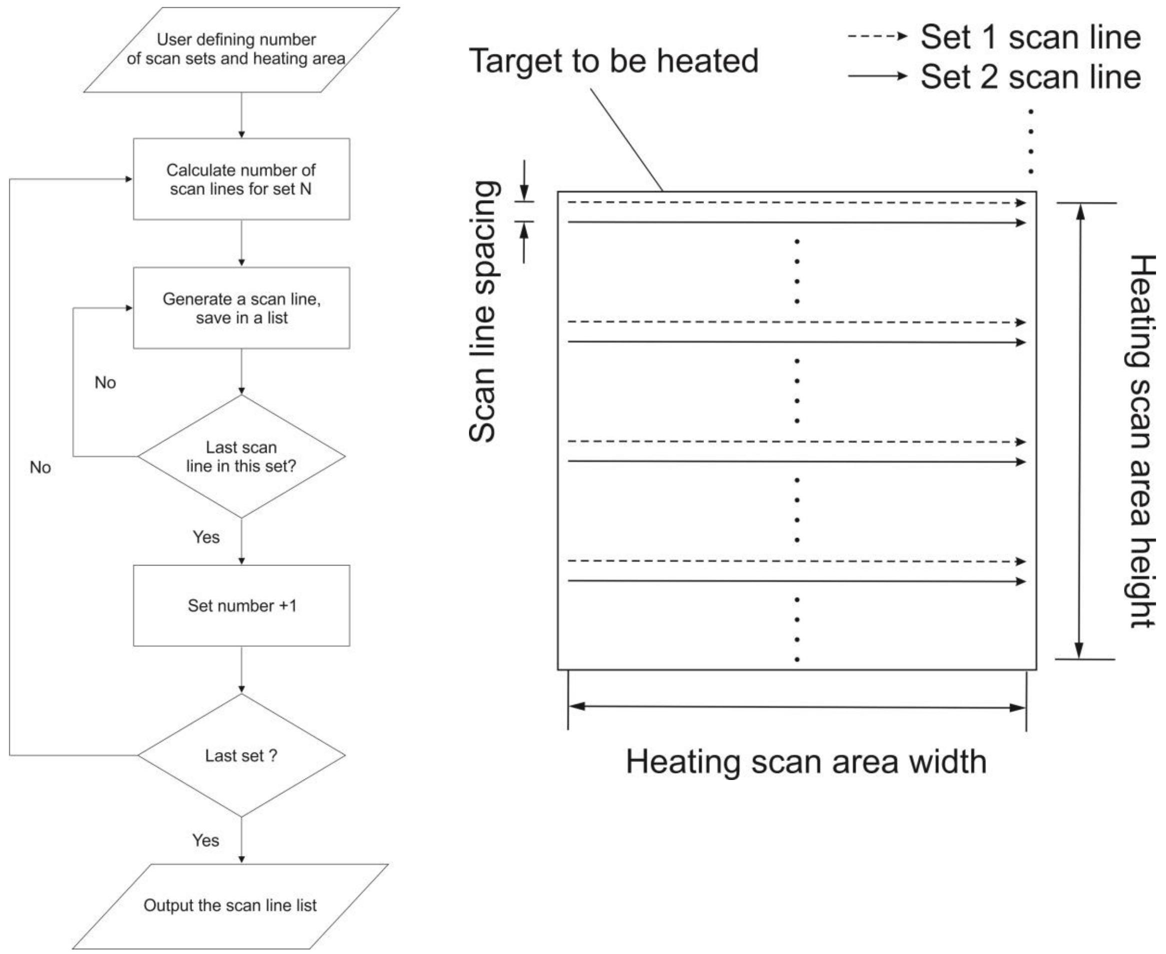

(a) Algorithm process flow chat (b) Typical scan line output

Fig. 3 Controlled heating algorithm

A verification trial was conducted upon completion of the heating algorithm development. The algorithm was applied to the EBM machine and the machine electron beam was used to heat up a stainless steel plate, i.e. heating target, by raster scanning across it in a pattern defined by the algorithm. Temperature data of the heating target was measured, processed and recorded by a thermocouple (TC), TC amplifier and a microcontroller respectively. Fig. 4(a) and (b) show the verification setup. Fig. 4(a) shows how the heating target, TC and microcontroller are connected to each other. Fig. 4(b) shows the design of the stainless steel plate, used as both a heating target in the verification trial and an imaging target in the imaging trials at a later stage. This plate, hereafter referred to as target plate, was made of one single material to avoid non-uniform deformation due to differences in thermal expansion coefficient during heating. Nine location markers and 27 pockets of $5mm$ in depth were machined across the plate. These features were used to develop image contrast during electronic imaging, allowing image quality to be evaluated. Prior to the verification trial, the target plate was processed as part of the development of the heating algorithm. Multiple pilot heating scans with various electron beam parameters were carried out across the middle of the plate. These developmental activities led to surface damage. During pilot electron beam heating, the beam traced out the target plate, leaving horizontal markings behind. In an attempt to undo the damage, the target plate was bead blasted manually with the Guyson Formula 1200 blast system (Guyson, UK), with 60-80 grit aluminium oxide abrasive to smooth out its surface texture.

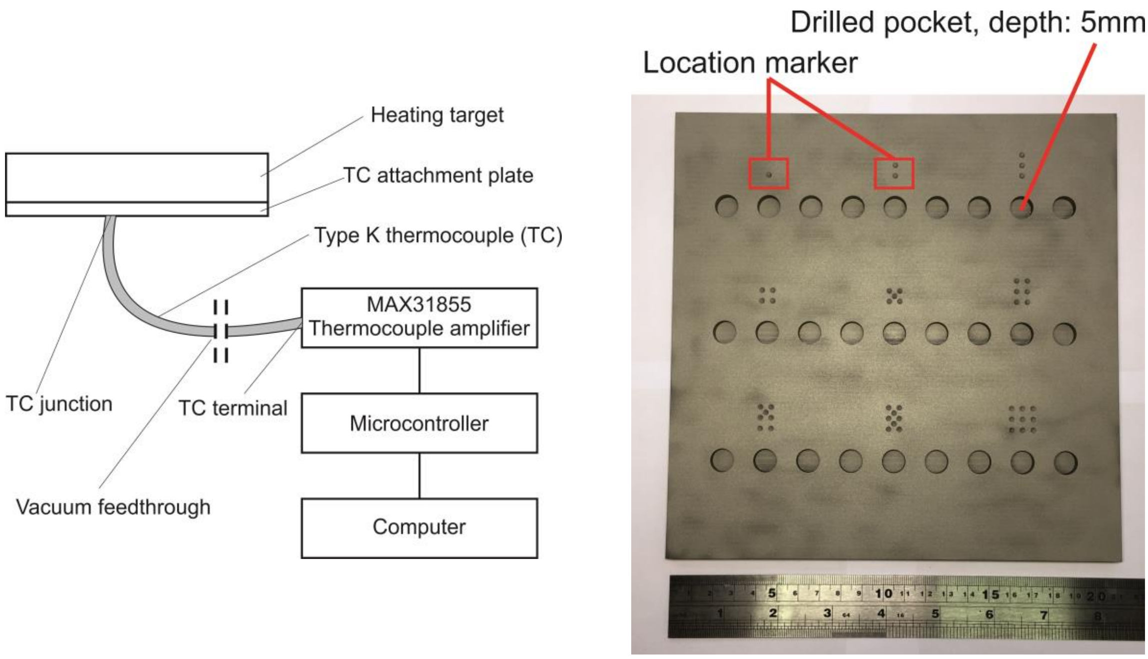

(a) Schematic of the setup (b) The heating target plate

Fig. 4 Heating algorithm verification setup

Table 3 details the controlled heating verification trial configuration. The electron beam speed, current and focus offset are chosen based on the beam parameters from the EBM machine standard pre-heating theme. $700°C$ is the maximum temperature goal. Fig. 5 shows the heating sequence generated by the controlled heating algorithm for the verification of the software.

Table 3 Controlled heating verification trial configuration

Controlled Heating Verification Trial Parameters	Value
Heating target dimension (mm^3)	210 × 210 × 10
Heating target material	Stainless steel
TC attachment plate dimension (mm^3)	200 × 200 × 2
TC attachment plate material	Stainless steel
Heating area (mm^2)	200 × 200
Scan line spacing (mm)	2.5
Number of scan lines per heating sequence	1760
Duration of each heating sequence (s)	10
Electron beam heating current (mA)	48
Electron beam heating focus offset (mA)	80
Electron beam heating scan speed (mms^{-1})	35000
Goal maximum temperature (°C)	700

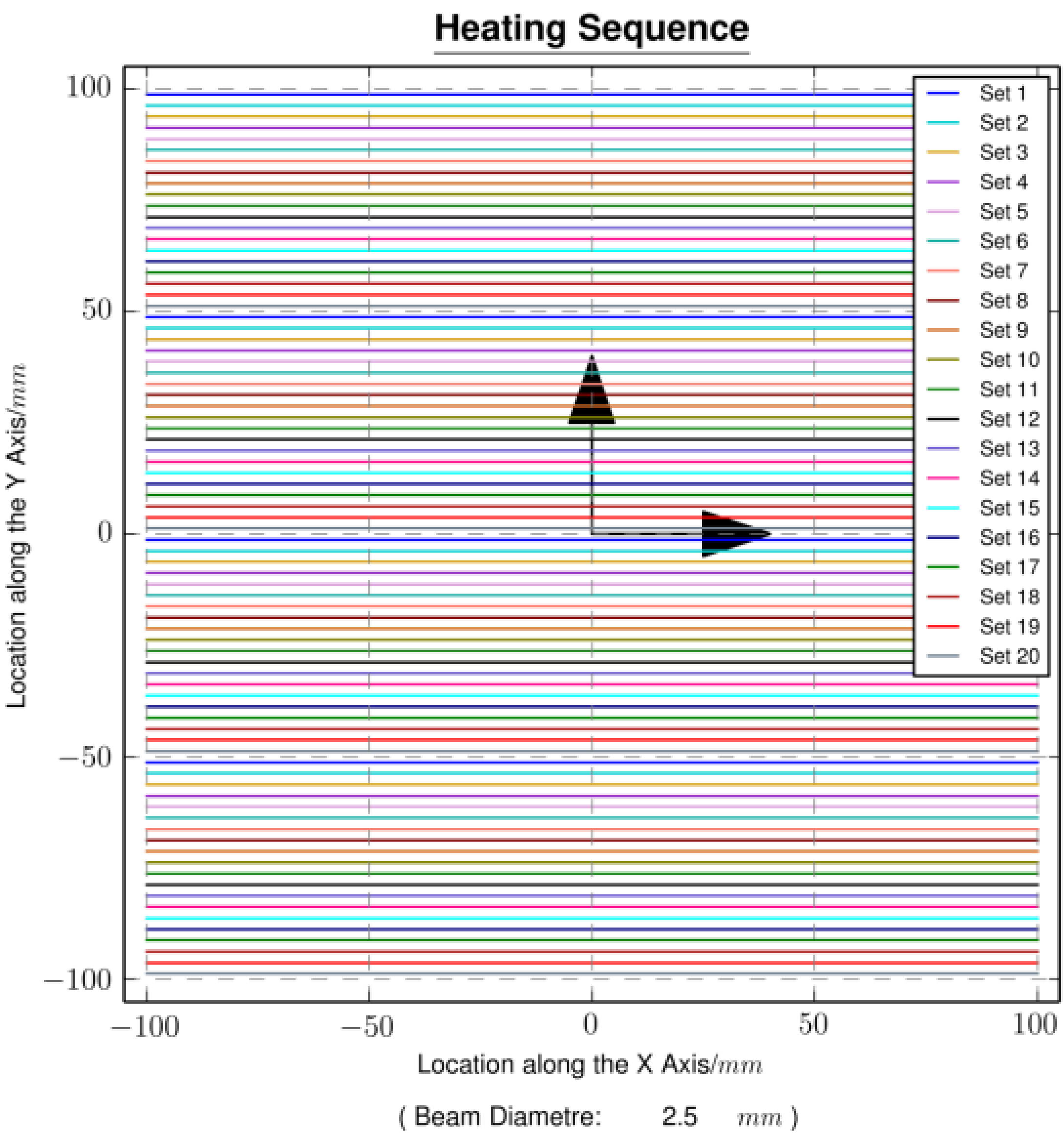

Fig. 5 Verification heating sequence generated by the controlled heating algorithm

In the verification trial, the target plate was successfully heated from room temperature to $700°C$ as shown in Fig. 6. The trial result demonstrates that the controlled heating algorithm is capable of bringing the target plate temperature up to the in-process EBM monitoring temperature for Ti-6Al-4V.

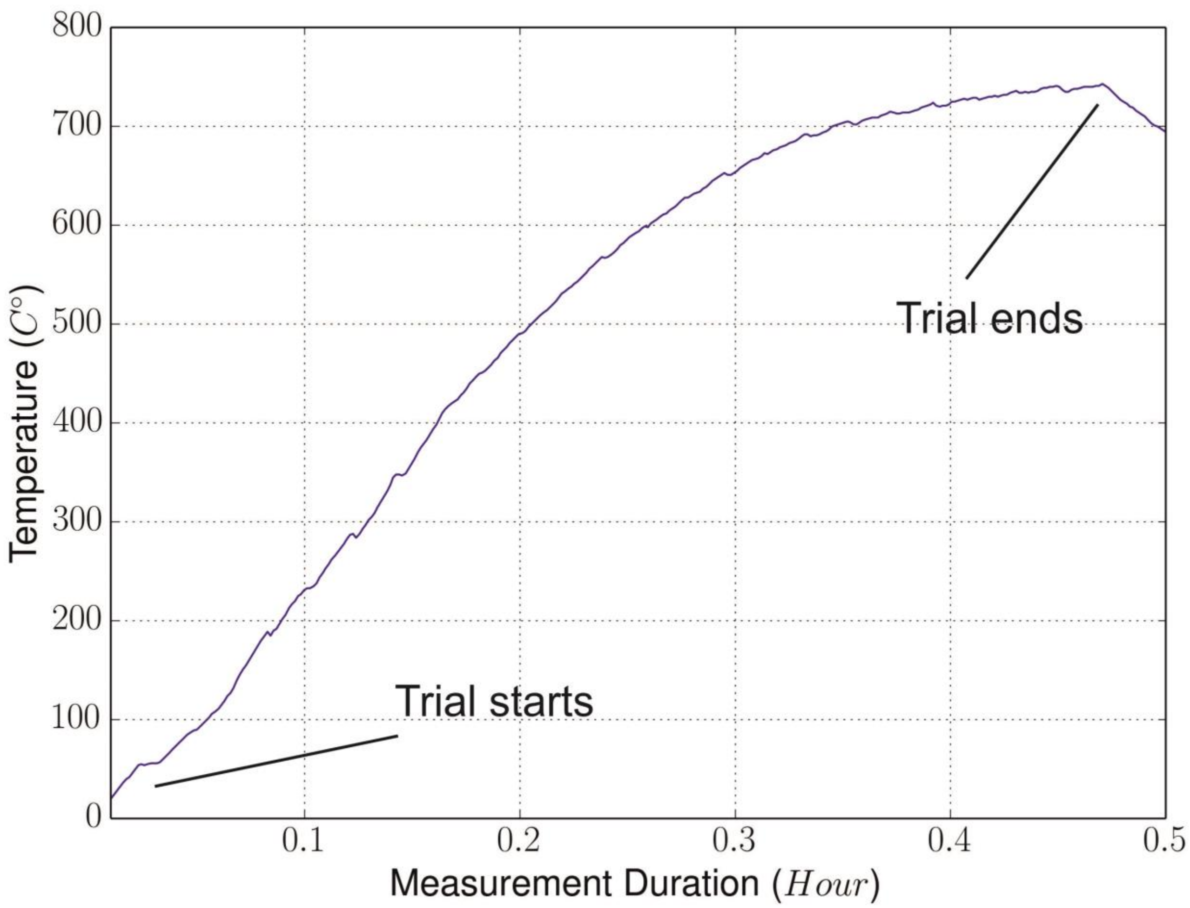

Fig. 6 Target plate temperature profile during controlled heating sequence verification

2.3 Electronic Image at Elevated Temperatures Experimental Setup

Upon successful verification of the controlled heating algorithm, electronic imaging was carried out at elevated temperatures with the electronic imaging system prototype and the EBM machine shown in Fig.1(a) and (b). The target plate shown in Fig. 4(b) was used as an imaging target. The verification temperature measurement setup (Fig.4(a) and (b)) and controlled heating configuration (Table 3) were used to bring up the imaging target temperature during the experiment. Table 4 gives the experimental configuration of the prototype and the EBM machine. The list below gives an overview of the experimental steps carried out:

1. Heat up target plate to a selected, intermediate temperature
2. Screenshots of the EBM machine computer taken, with chamber light switched on/off (images captured by the machine near-IR camera)
3. Electronic imaging conducted with machine chamber light switched off

Preprints (www.preprints.org) | NOT PEER-REVIEWED | Posted: 10 January 2019 doi:10.20944/preprints201901.0098.v1

Table 4 Prototype and EBM machine configurations for imaging at elevated temperatures

Imaging Experiment Parameters	Value
Machine chamber vacuum level (mbar)	10^{-3}
Electron beam imaging current (mA)	1
Electron beam imaging scan speed (mms^{-1})	11880
Electron beam imaging focus offset (mA)	0
Signal amplifier gain	10
Data logger input / output range (V)	$0\ to + 3.3$
Data logger sampling frequency (Hz)	$118.8k$
Sample resolution (bit)	8
Data logger sampling bit rate (bps)	$950.4k$
Imaging area (mm^2)	180×180
Image size ($pixel^2$)	1800×1800
Image bit depth	256
Imaging temperatures ($\pm$10°C)	$30/200/350/450/700$

3. Results

3.1 Imaging Target Temperature Profile during Experiment

Target plate temperature was monitored by a TC and its peripheral electronics during the experiment. Fig. 7 depicts the target plate temperature profile. It shows that the target plate temperature ramps up from room temperature to up until $700°C$. The figure illustrates that electronic images are generated at five different temperatures throughout the experiment.

Preprints (www.preprints.org) | NOT PEER-REVIEWED | Posted: 10 January 2019 doi:10.20944/preprints201901.0098.v1

Negative temperature gradients may be observed during imaging, indicating that the target plate temperature drops. The figure also demonstrates that the rate of temperature drop increases as temperature rises.

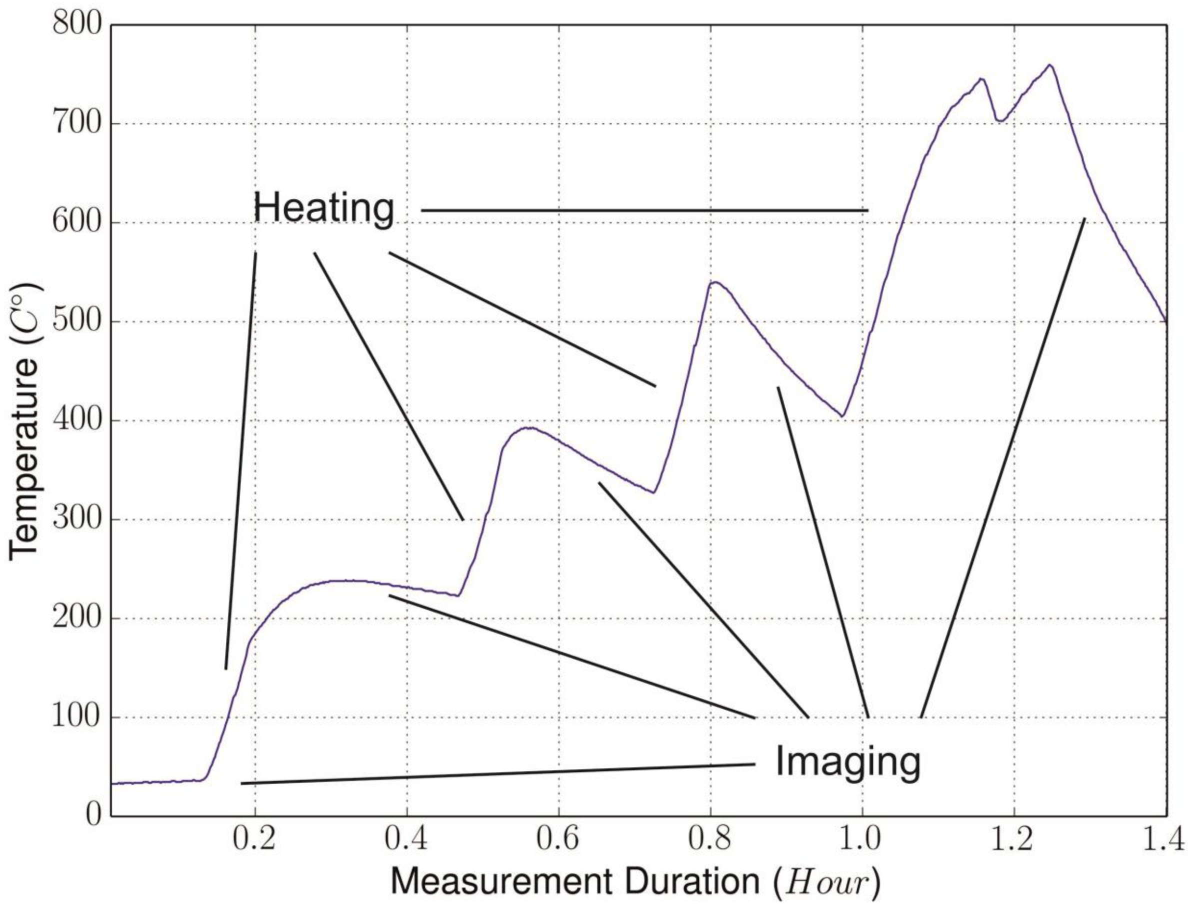

Fig. 7 Target plate temperature profile during electronic imaging experiment

3.2 Near-IR Images from the Arcam A1 EBM Machine Camera

During experiment, screenshots of the EBM machine computer were captured at various elevated temperatures to demonstrate the quality of typical thermal/optical images. Fig. 8(a)-(d) are the typical screenshots captured. Fig. 8(a) and (b) were captured at 30±10°C with the chamber light switched off and on; Fig. 8(c) and (d) were captured at 650±10°C with the chamber light switched off and on. A bright circular spot in the centre of the target plate can be observed in Fig. 8(a) and (c), when the chamber light was switched off. The bright spot is no longer visible when the chamber light is on, as demonstrated by Fig. 8(b) and (d).

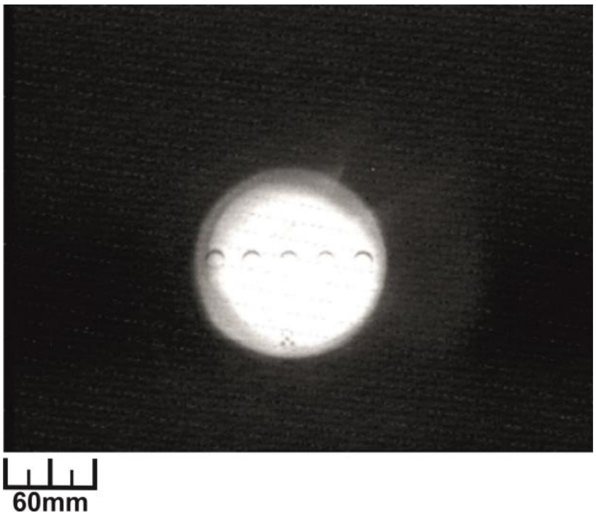

(a) 30±10°C, light off

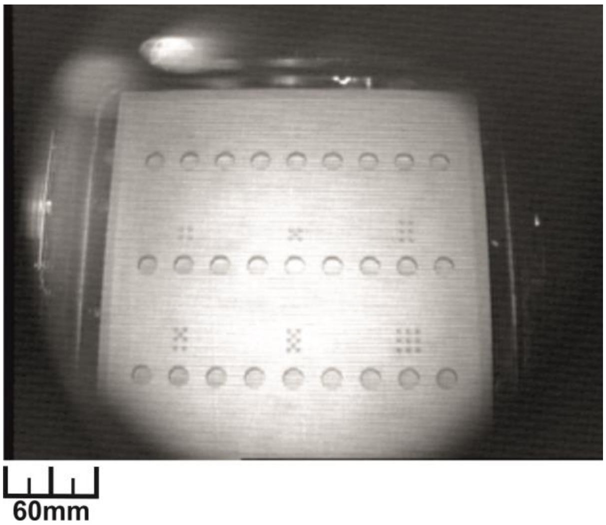

(b) 30±10°C, light on

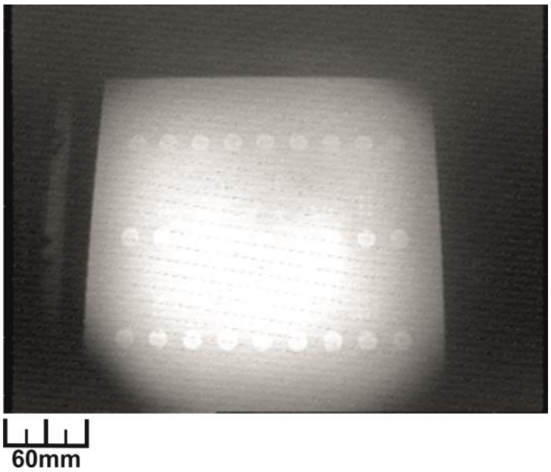

(c) 650±10°C, light off

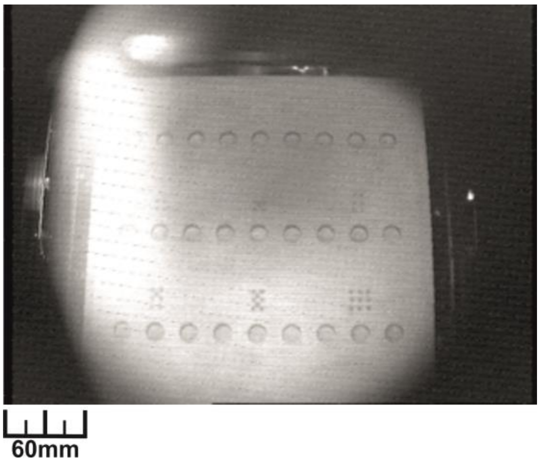

(d) 650±10°C, light on

Fig. 8 EBM machine computer screenshots of a target plate taken from the machine near-IR camera at various temperatures and lighting conditions

3.3 Digital Image Processing

Raw digital electronic images were generated from the electronic imaging experiment. In order to generate processed electronic images, noise was removed by applying a median filter, and image contrast was enhanced by carrying out histogram equalisation. Eq. 3 [32] and Eq. 4 [32] define the median filter and histogram equalisation functions used respectively. The median filter applied had a user-defined neighbourhood area of a circle with radius of two pixels. The histogram equalisation was carried out with a user-defined saturated pixel value of 0.3%, allowing 0.3% of the total pixels to become saturated.

$$\hat{f}(x,y) = \underset{(s,t)\in S_{xy}}{median}\{g(s,t)\} \tag{3}$$

Where

$\hat{f}$ (x,y) is the pixel-value of the filtered image at (x,y), g(s,t) is the pixel-value of the raw image at (s,t), and S_{xy} represents the set of coordinates within a user-defined area of an image

$$y_k \triangleq \left\lfloor \left\lfloor (L-1)\sum_{i=0}^{k} h(i) \right\rfloor + 0.5 \right\rfloor \qquad k = 0, 1, 2, \ldots\ldots, L-1 \tag{4}$$

Where

L is the bit-depth in an image, k is the pixel-value within the bit-depth, L, h(i) is the normalised histogram which gives the probability of occurrence of pixel-value, I, $\sum_{i=0}^{k} h(i)$ is the cumulative probability distribution of the normalised histogram, and y_k is an integer, the equalised number of pixel with a pixel-value of k

3.4 Electronic Images from the Prototype

Electronic imaging was conducted at five elevated temperatures, covering a range of $30°C$ to $650°C$. Five electronic images were generated at each temperature. Fig. 9(a)-(e) presents the typical raw electronic images generated. Fig. 10(a)-(e) on the other hand, present the typical processed electronic images with noise removed and contrast enhanced. The two processed electronic images generated at 30±10°C (Fig. 10(a)) and 200±10°C (Fig. 10(b)) show a darker area across the middle of the target plate.

Preprints (www.preprints.org) | NOT PEER-REVIEWED | Posted: 10 January 2019 doi:10.20944/preprints201901.0098.v1

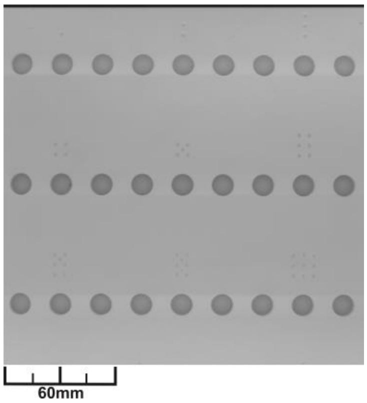

(a) 30±10°C

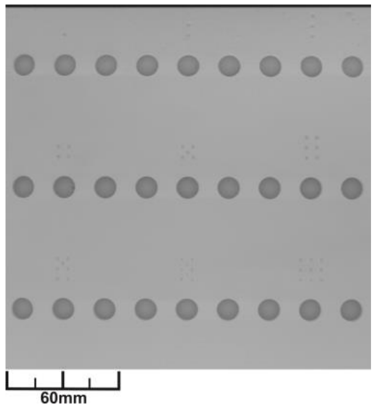

(b) 200±10°C

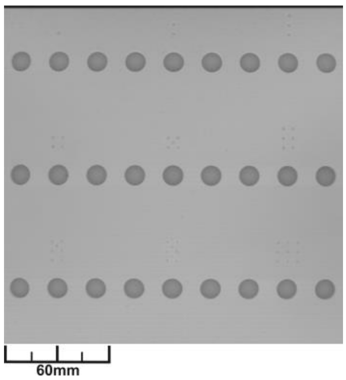

(c) 350±10°C

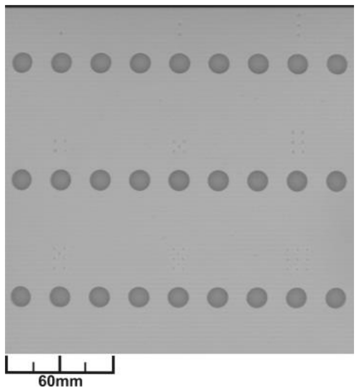

(d) 450±10°C

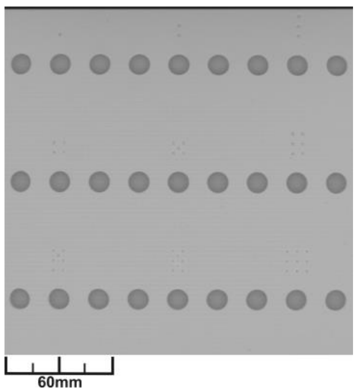

(e) 650±10°C

Fig. 9 8-bit, 1800 $pixel \times 1800\ pixel$ $(row \times column)$ digital electronic images (raw) covering an imaging area of $180mm \times 180mm$ $(W \times D)$ in the EBM machine processing area, generated at various temperatures with chamber light off

Preprints (www.preprints.org) | NOT PEER-REVIEWED | Posted: 10 January 2019 doi:10.20944/preprints201901.0098.v1

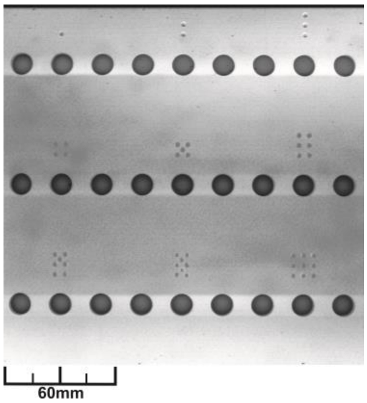

(a) 30±10°C

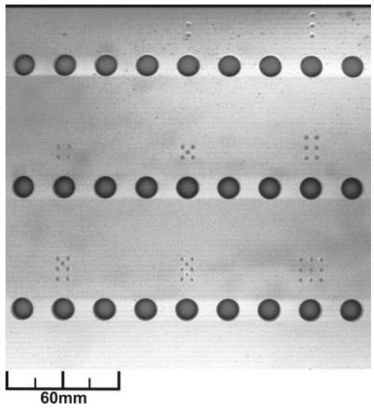

(b) 200±10°C

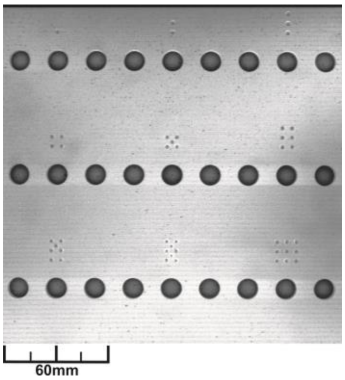

(c) 350±10°C

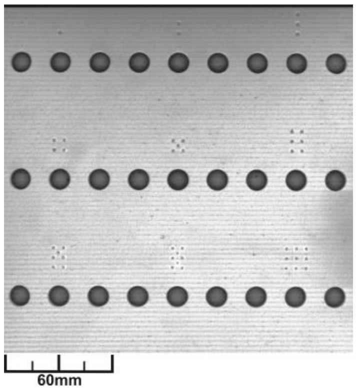

(d) 450±10°C

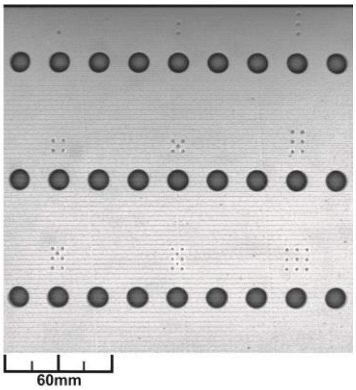

(e) 650±10°C

Fig. 10 8-bit, 1800 $pixel \times 1800\ pixel\ (row \times column)$ digital electronic images (processed) covering an imaging area of $180mm \times 180mm\ (W \times D)$ in the EBM machine processing area, generated at various temperatures, with chamber light off

3.5 Local Image Quality Comparison between Near-IR and Electronic Images

This section presents a qualitative comparison on local image quality between an EBM machine near-IR image and a prototype electronic image. Only a local feature, i.e. the image contrast between the target plate surface and drilled pockets, is examined. The purpose of this comparison is neither to present any statistically significant observations nor advocate the supremacy of electronic images over thermal/optical images on a quantitative basis. This comparison only aims to give an overview on local image quality between the two types of images.

A typical near-IR image and electronic image captured and generated at $650 \pm 10°C$ are presented as Fig. 11(a) and (c). These two images are annotated with a red line along their bottom rows crossing the drilled pockets. Fig. 11(b) and (d) are the pixel value profiles along their red lines.

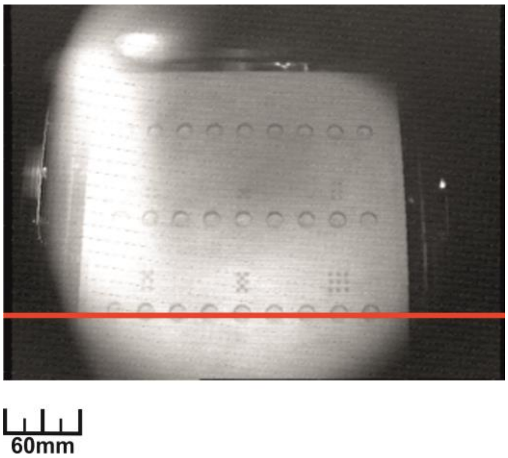

(a) Near-IR image

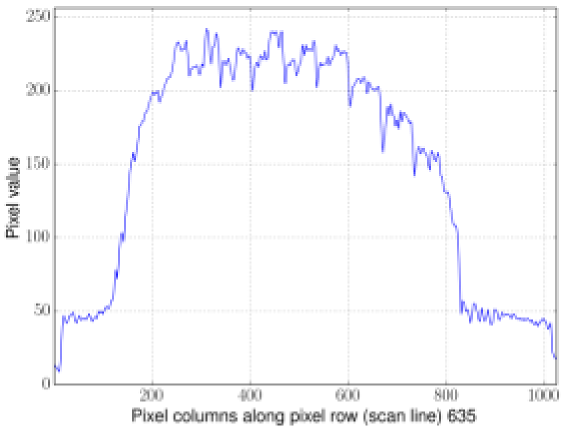

(b) Pixel values along the red line (near-IR)

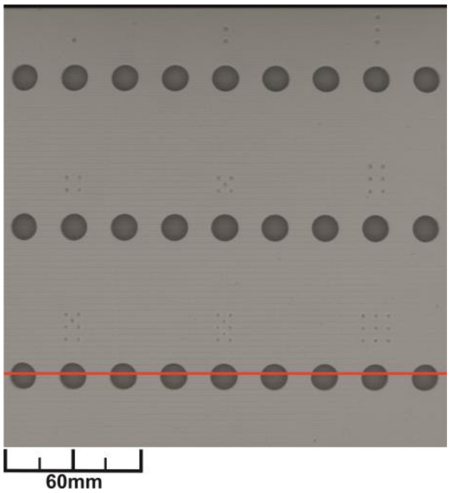

(c) Electronic image (raw)

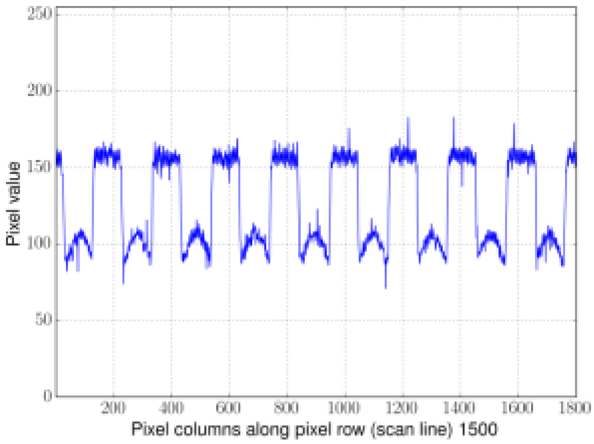

(d) Pixel values along the red line (electronic)

Fig. 11 Near-IR and electronic images taken at 650±10°C, with light on

3.6 Global Image Quality Measure Q Evaluation on Electronic Images

The influence of temperature and thermal noise on electronic image was investigated, and quantitative analysis on the global quality of electronic images generated at various elevated temperatures was carried out. Reiter et al [33] describe an image quality measure Q in their studies on histogram-based images, as defined by Eq. 5 and Fig. 12.

Preprints (www.preprints.org) | NOT PEER-REVIEWED | Posted: 10 January 2019 doi:10.20944/preprints201901.0098.v1

$$Q = \frac{|\mu_2 - \mu_1|}{\sqrt{\sigma_1^2 + \sigma_2^2}} \tag{5}$$

Where

Q is the image quality measure, μ_i is the within-class mean, $i = 1, 2$, the pixel value class present, and σ_i is the within-class standard deviation, $i = 1, 2$, the pixel value class present

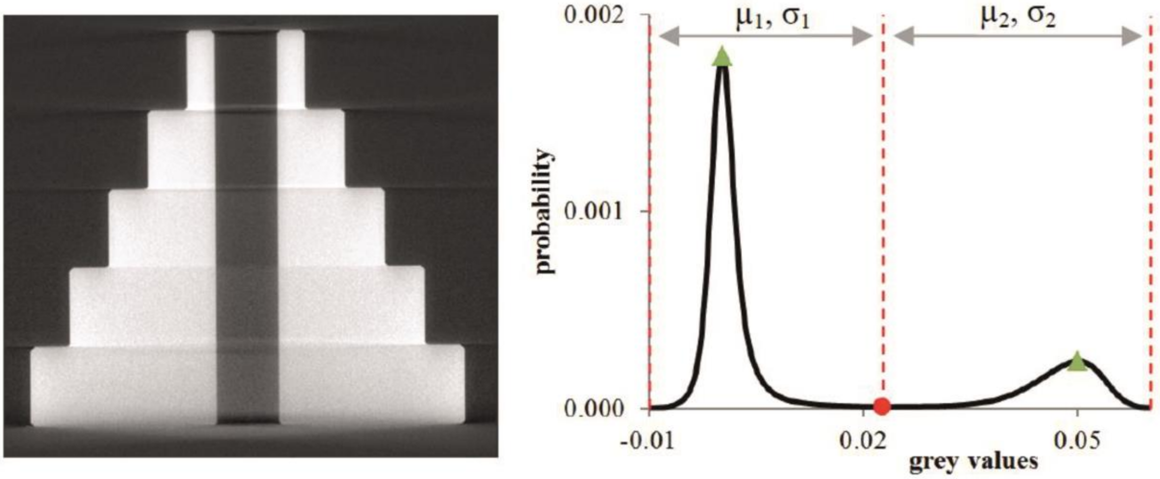

Fig. 12 A demonstration image and its bimodal histogram showing the definitions of threshold, within-class mean and within-class standard deviation [33]

This image quality measure Q represents the degree of separation between the two pixel value classes in the histogram of interest. An image of ideal global quality is defined to consist of minimum noise and blur throughout the whole image. The separation of the classes within this histogram are maximised whilst the classes' within-class standard deviations are minimised. As the measure Q takes into account both noise and blur, it gives a global impression of image quality. The greater the Q value, the better the global image quality.

A total of ten sets of histograms were assessed in this Q value evaluation. Five sets were generated from raw electronic images while the other five from processed electronic images. Each set contains five histograms. Table 5 and 6 summarise the formation of the ten histogram sets.

Table 5 The five raw histogram sets involved in image quality measure Q analyses

Histogram Set	Number of Histograms in a Set	Representative Figure	Temperature / $°C$
Raw_30	5	9(a)	30$\pm$10
Raw_200	5	9(b)	200$\pm$10
Raw_350	5	9(c)	350$\pm$10
Raw_450	5	9(d)	450$\pm$10
Raw_650	5	9(e)	650$\pm$10

Table 6 The five processed histogram sets involved in image quality measure Q analyses

Histogram Set	Number of Histograms in a Set	Representative Figure	Temperature / $°C$
Procssed_30	5	10(a)	30$\pm$10
Processed_200	5	10(b)	200$\pm$10
Processed_350	5	10(c)	350$\pm$10
Processed_450	5	10(d)	450$\pm$10
Processed_650	5	10(e)	650$\pm$10

Otsu thresholding [34] was applied to the ten histogram sets to estimate their pixel value classification thresholds. Thresholding was then followed by the analysis of global image quality measure Q of the histograms.

Results of the Q values are summarised in Table 7 and 8. The average within-class pixel value means ($\mu_{,avg}$), average within-class standard deviations ($\sigma_{,avg}$), average Q (Q_{avg}) values and standard errors are presented. Fig. 13 is a visual representation of results in Table 7 and 8. Although the standard errors are plotted as error bars on Fig. 13, due to their low values, they are not visible. Fig. 13 indicates that the processed electronic images have lower Q values, i.e. poorer global image quality, when compared to that of raw images. From a qualitative perspective, a slight increase in Q values can be observed in both raw and processed images, with increasing imaging temperature.

Table 7 Global image quality measure Q analyses. Data rounded to 3 s.f.

Histogram Set	$\mu_{1,avg}$	$\mu_{2,avg}$	$\sigma_{1,avg}$	$\sigma_{2,avg}$	Q_{avg}	Standard Error
Raw_30	86.8	146	26.5	8.07	2.12	0.0193
Raw_200	84.3	142	24.5	6.02	2.30	0.00355
Raw_350	87.1	147	24.5	6.75	2.36	0.00200
Raw_450	86.2	148	23.9	7.34	2.46	0.00223
Raw_650	87.6	3.03	24.3	7.71	2.52	0.01334

Table 8 Global image quality measure Q analyses. Data rounded to 3 s.f.

Histogram Set	$\mu_{1,avg}$	$\mu_{2,avg}$	$\sigma_{1,avg}$	$\sigma_{2,avg}$	Q_{avg}	Standard Error
Processed_30	112	198	34.7	27.3	1.95	0.0187
Processed_200	110	194	38.3	27.5	1.77	0.00322
Processed_350	108	199	39.1	26.2	1.94	0.0102
Processed_450	95.0	200	39.6	27.2	2.19	0.00957
Processed_650	95.6	204	39.9	26.5	2.25	0.00652

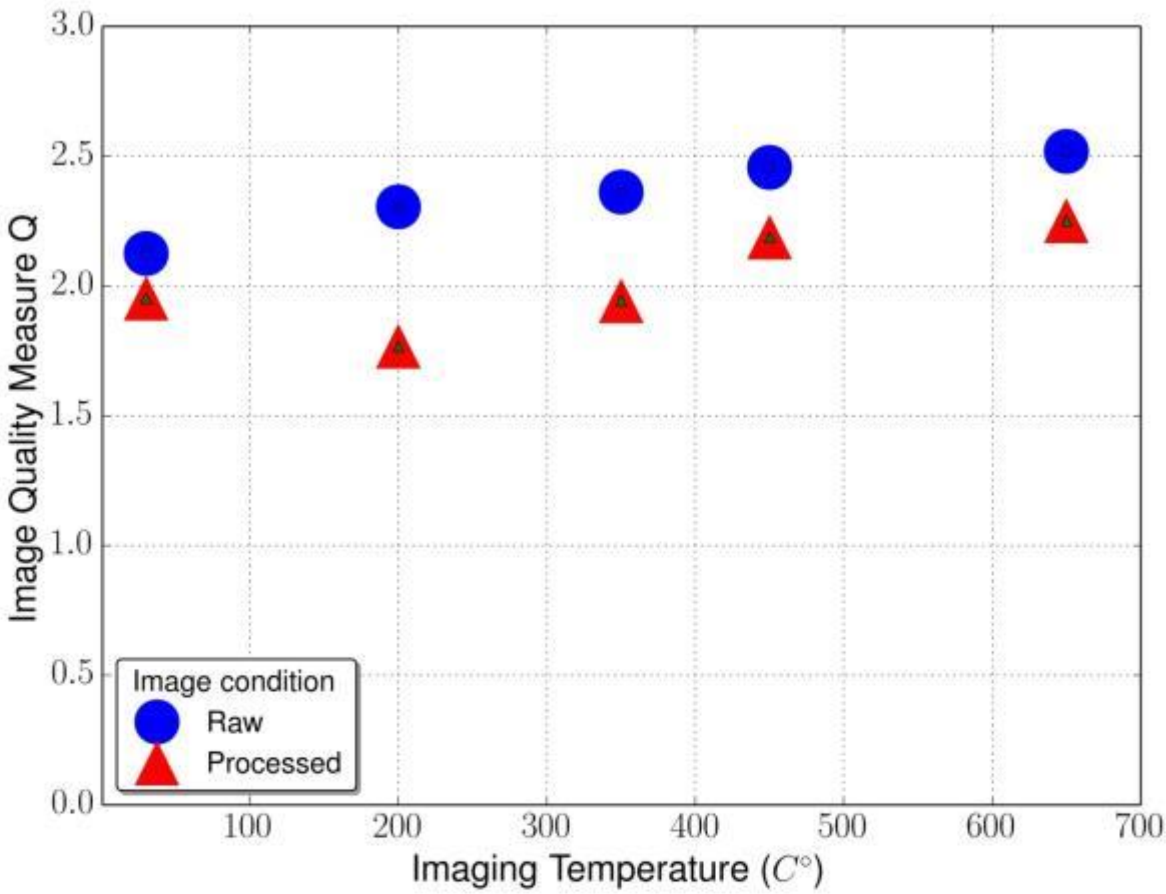

Fig. 13 A Global image quality measure Q of raw and processed electronic images generated at various elevated temperatures

Discussion

4.1 Digital Image Generation at Elevated Temperatures

Fig. 7 shows the target plate temperature profile measured. Negative heating rates (negative gradients) are observed from Fig. 7 when electronic imaging is carried out. Moreover, the heating rate becomes more negative (greater gradient, steeper slope) as the target temperature increases. Firstly, this suggests that the target plate struggles to maintain a constant temperature during the experiment. The EBM machine has a controlled vacuum system in which helium gas is admitted into the machine to maintain the $10^{-3} mbar$ operational chamber pressure as described in Table 4. It is thought that during controlled heating of the target plate, heat was lost to the machine chamber and the machine surrounding via convection and conduction. According to Newton's law of cooling (Eq. 6 [35]), the heat transfer rate $\dot{Q}_{conv}$ increases with an increasing temperature difference. As the target plate becomes hotter, the temperature difference between itself and the machine chamber and surrounding environment increases, thus leading to a greater $\dot{Q}_{conv}$. As the amount of activity carried out during each imaging trial (as described in Section 2.3) is the same, it is expected that the time involved in imaging will be similar. With similar imaging time and an increasing $\dot{Q}_{conv}$ at higher temperature, the temperature drops are expected to be greater at higher temperatures. The profile of the target plate depicted in Fig. 7 has been explained.

$$\dot{Q}_{conv} = hA(T_s - T_f) \tag{6}$$

Where

$\dot{Q}_{conv}$ is the heat transfer rate by convection, h is the convection heat transfer coefficient

A is the surface area involved in heat transfer, and Ti is the temperature of s = surface and f = bulk fluid, $i = s, f$

4.2 Electronic Images from the Prototype

Fig. 9(a)-(e) and Fig. 10(a)-(e) are the typical raw and processed electronic images generated at various elevated temperatures. A black line is present at the top of all raw and processed images. Delays in the delivery of electron beam current from the EBM machine electron gun is thought to be the root cause, as mentioned in literature [22].

Fig. 10(a) and (b) show a darker middle area when compared to the rest of the image areas. This observation suggests a difference in surface texture between the middle and the rest of the target plate. It is thought that the texture variation comes from the manual bead blasting described in Section 2.2. Bead blasting was focused on the middle of the target plate, in order to smooth out the horizontal markings left behind from the developmental trials prior to the imaging experiment. Fig. 10(c)-(e) do not contain any dark areas in the middle of the plate. Fig. 7, the target plate temperature profile shows that the plate goes through multiple heating sequences for 0.6±0.1, 0.9±0.1 and 1.3±0.1 hours before reaching temperature of 350±10°C, 450±10°C and 650±10°C, when Fig. 10(c)-(e) were generated. It is thought that the controlled heating via electron beam scanning modified the target plate surface texture throughout the experiment, smoothing out the variation in surface texture. This argument is supported by the fact that horizontal markings across the target plate become more and more visible from Fig. 10(a)-(e), as the imaging temperature increases. As a result, the surface texture variation due to bead blasting at the start of the experiment is no longer present, by the time that images shown in Fig. 10(c)-(e) were generated.

4.3 Comparison between Near-IR Images and Electronic Images

Fig. 8(a)-(d) are EBM machine computer screenshots of near-IR images taken by the machine camera at 30±10°C (Fig. 8(a) and (b)) and 650±10°C (Fig. 8(c) and (d)). The bright spots in Fig. 8 (a) and (c) are thought to be attributed to incandescence of the electron gun cathode. The EBM machine has a thermionic electron gun [36], and when the tungsten cathode is heated, it emits blackbody radiation according to Planck's law [37]. The bright spot in Fig. 8(c) is less visible as the target plate is brighter when compared to that in Fig. 8(a). This occurs when the target plate is at 650±10°C, and glows as predicted by Planck's law. When the machine chamber light was turned on, the image contrast due to incandescence was less obvious, as demonstrated by Fig. 8(b) and (d). The effect of cathode incandescence is thought to be a potential issue with thermal / optical imaging systems. These systems rely on the correct operation of the machine chamber light. If the chamber light malfunctions, the quality of the images captured during in-process data collection is compromised.

Fig. 9(a)-(e) show typical raw digital electron images generated at a range of temperatures, with the chamber light switched off. These images demonstrate that cathode incandescence does not influence the electronic image quality. This occurs because the energy of the electron cathode blackbody radiation is caused by photons, the electron sensor in the prototype only registers electrons impinging onto its sensing surface. This blackbody radiation is invisible to the electronic imaging system.

In comparison with near-IR images of Fig. 8(a)-(d), the image FOV of the digital electronic images of Fig. 9(a)-(e) only consist of a user-defined 180 mm ×180 mm (W×D) Regions of Interest (ROI), without including any other monitoring-irrelevant regions beyond the machine processing area. Thus, all image pixels are carrying useful information for monitoring.

When compared with the near-IR image of Fig. 11(a), the electronic image of Fig. 11(c) reveals more topographical details of the target plate. Fig. 11(c) shows the drilled pockets with greater clarity when compared to Fig. 11(a). From a qualitative perspective, this observation is supported by Fig. 11(d), the contrast in pixel value is better-defined when compared to that in Fig. 11(b).

4.4 Global Image Quality Measure Q Evaluation on Electronic Images

A total of ten sets of histograms (five images per set) were assessed in the Q value evaluation. Fig. 13, in which standard errors are plotted as error bars, shows that the standard errors of all images involved are insignificant as the error bars are not visible. This indicates that for each image set, the five electronic images generated at each elevated temperature are similar in quality.

Fig. 13 demonstrates that the Q values of raw images are greater than that of the processed images. This indicates that global image quality of the raw images is higher. As discussed in Section 3.3, processed images are generated by applying noise removal and contrast enhancement to the raw images. The contrast enhancement amplifies the local pixel intensity variations in the raw images. Although the enhancement leads to greater difference between the two within-class means (μ_1 and μ_2), the sum of the within-class standard deviations (σ_1 and σ_2) are even greater. Thus, the resultant Q value drops after image processing is carried out (refer to Eq. 5).

Still referring to Fig.13, a gradual increase in Q value with higher imaging temperature can be observed for both raw and processed images, indicating that the global image quality increases with higher temperature. This phenomenon is thought to be mainly due to the undesired surface texture variation across the target plate at the start of the experiment. As referenced in Section 2.2 and 4.2, the electron beam scanning motion during controlled heating is believed to have modified the target plate surface texture. As the experiment proceeds, more electron beam scanning is carried out, bringing up the target plate temperature, and the initial target plate surface texture variation becomes smoother. Consequently, with higher imaging temperature, the global image quality improves.

5. Conclusions

Electron signal amplifier modification, controlled heating algorithm development and experimental setup for carrying out electronic imaging trials at elevated temperatures have been presented. Near-IR (EBM machine standard camera) and electronic images (self-developed prototype) were captured and generated at temperatures covering a range of $30°C$

to $650°C$. When compared with near-IR images, electronic images show that they have better-defined image FOV, and are not affected by cathode incandescence. Global image quality measure Q analysis was carried out on both raw and processed electronic images to evaluate the influence of temperature on image quality. Electronic images generated in the experiment have low standard error, showing that their image quality is consistent. Moreover, electronic images generated at higher temperatures have greater Q value, i.e. better global image quality. This difference is mainly attributed to the undesired surface texture variation of the imaging target due to electron beam heating. At the start of the experiment, the imaging target contained an undesirable, inhomogeneous surface texture. Scanning of the electron beam during heating is thought to have homogenised the surface texture, thus leading to higher Q values of images. It has been demonstrated that, for temperature in the range of $30°C - 650°C$, the influence of temperature on electronic image quality is minimal. It is envisaged that the prototype under test has significant potential to contribute to in-process EBM monitoring in many manufacturing sectors, including the aerospace and medical device industries. There will, however, be challenges ahead in order to realise the prototype potential. Future studies will focus on these issues which include: carrying out electronic imaging on multi-layer for the whole additive manufacturing process, and resolving sensor issues due to metallisation generated from vaporisation of metal powder during the EBM process.

Acknowledgements

The Author(s) declare(s) that there is no conflict of interest. This research received no specific grant from any funding agency in the public, commercial, or not-for-profit sectors. The EBAM machine was purchased, in part from a grant received for the EPSRC Centre for Innovative Manufacturing in Additive Manufacturing.

References

1. I. Gibson, D.W. Rosen, B Stucker (2010) Additive Manufacturing Technologies. Springer, New York, pp. 126-128

2. X Gong, T Anderson, K Chou (2014) Review on Powder-Based Electron Beam Additive Manufacturing Technology. Manufacturing Review 1 2. DOI: 10.1051/mfreview/2014001

3. O.L.A Harrysson, O. Cansizoglu, D.J. Marcellin-Little, D.R Cormier, H.A West (2008) Direct Metal Fabrication of Titanium Implants with Tailored Materials and Mechanical Properties using Electron Beam Melting Technology, Materials Science and Engineering: C, Volume 28, Issue 3, 2008, Pages 366-373, ISSN 0928-4931, http://dx.doi.org/10.1016/j.msec.2007.04.022.

4. G. Baudana, S. Biamino, D. Ugues, M. Lombardi, P. Fino, M. Pavese, C. Badini, (2016) Titanium Aluminides for Aerospace and Automotive Applications Processed by Electron Beam Melting: Contribution of Politecnico di Torino, Metal Powder Report, Volume 71, Issue 3, 2016, Pages 193-199, ISSN 0026-0657, http://dx.doi.org/10.1016/j.mprp.2016.02.058.

5. J.P. Jarow, J.H. Baxley (2015) Medical devices: US Medical Device Regulation, Urologic Oncology: Seminars and Original Investigations, Volume 33, Issue 3, March 2015, Pages 128-132, ISSN 1078-1439, https://doi.org/10.1016/j.urolonc.2014.10.004.

6. L. Portolés, O. Jordá , L. Jordá, A. Uriondo, M. Esperon-Miguez, S. Perinpanayagam (2016) A qualification Procedure to Manufacture and Repair Aerospace Parts with

Electron Beam Melting, Journal of Manufacturing Systems, Volume 41, 2016, Pages 65-75, ISSN 0278-6125, http://dx.doi.org/10.1016/j.jmsy.2016.07.002.

7. M. Mani, B. Lane, A. Donmez, S. Feng, S. Moylan, R. Fesperman (2015) NISTIR 8036. Measurement Science Needs for Real-time Control of Additive Manufacturing Powder Bed Fusion Processes. http://dx.doi.org/10.6028/NIST.IR.8036

8. J. Raplee, A. Plotkowski, M.M. Kirka, R. Dinwiddie, A. Okello, R.R. Dehoff, S.S Babu (2017) Thermographic Microstructure Monitoring in Electron Beam Additive Manufacutirng, Scientific Reports 7, Article Number: 43554. doi:10.1038/srep43554

9. P.M. Cordero, J. Mireles, S. Ridwan, R.B. Wicker (2017) Evaluation of Monitoring Methods for Electron Beam Melting Powder Bed Fusion Additive Manufacutirng Technology, Progress in Additive Manufacturing, June 2017, Volume 2, Issue 1-2, pp 1-10, https://doi.org/10.1007/s40964-016-0015-6

10. E. Rodriguez, F. Medina, D. Espalin, C. Terrazas, D. Muse, C. Henry, E. MacDonald, R. Wicker (2012) Integration of a Thermal Imaging Feedback Control System in Electron Beam Melting, Proceedings from the Solid Freeform Fabrication Symposium, pp 945–961

11. J.N. Zalameda, E.R. Burke, R.A. Hafley, K.M.B. Taminger, C.S. Domack, A. Brewer, R.E. Martin (2013) Thermal Imaging for Assessment of Electron-Beam Freeform Fabrication Additive Manufacturing Deposits, Proceeding of SPIE, Volume 8705, Thermosense: Thermal Infrared Applications XXXV, 87050M (2013), doi: 10.1117/12.2018233

12. S. Price, J. Lydon, K. Cooper, K Chao (2013) Experimental Temperature Analysis of Powder-Based Electron Beam Additive Manufacturing, Proceedings from the Solid Freeform Fabrication Symposium, pp. 162-173

13. S. Price, K. Cooper, K. Chou (2012) Evaluations of Temperature Measurmnets by Near-Infrared Thermography in Powder-Based Electron-Beam Additive Manufacturing, Proceedings from the Solid Freeform Fabrication Symposium, pp. 761-773

14. T. Scharowsky, A. Bauereiß, R.F. Singer, C. Körner (2012) Observation and Numerical Simulation of Melt Pool Dynamic and Beam Powder Interaction During Selective Electron Beam Melting, Proceedings from the Solid Freeform Fabrication Symposium, Austin, pp 815–820

15. S. Ridwan, J. Mireles, S.M. Gayton, D. Espalin, R.B. Wicker (2014) Automatic Layerwise Acquisition of Thermal And Geometric Data of The Electron Beam Melting Process Using Infrared Thermography, Proceedings from the Solid Freeform Fabrication Symposium, pp 343–352

16. J. Mireles, S. Ridwan, P.A. Motron, A. Hinojos, R.B. Wicker (2015) Analysis and Correction of Defects Within Parts Fabricated Using Powder Bed Fusion Technology. Surface Topography: Metrology and Properties, Volume 3, Number 3. doi:10.1088/2051-672X/3/3/034002

17. R.B. Dinwiddie, R.R. Dehoff, P.D. Lloyd, L.E. Lowe, J.U.B Ulrich (2013) Thermographic In-Situ Process Monitoring of the Electron-Beam Melting Technology Used in Additive Manufacturing, Proceeding of SPIE, Thermosense: Thermal Infrared Applications XXXV, 87050K; doi:10.1117/12.2018412

18. J. Schwerdtfeger, R.F. Singer, C. Körner (2012) In situ flaw detection by IR-imaging during electron beam melting, Rapid Prototyping Journal, Vol. 18 Issue: 4, pp.259-263, https://doi.org/10.1108/13552541211231572

19. J. Mireles, C. Terrazas, S.M. Gaytan, D.A. Roberson, R.B. Wicker (2015) Closed-Loop Automatic Feedback Control in Electron Beam Melting, Int J Adv Manuf Technol. 78: 1193. doi:10.1007/s00170-014-6708-4

20. J. Mireles, C. Terrazas, F. Medina, R. Wicker (2013) Automatic Feedback Control in Electron Beam Melting Using Infrared Thermography. Proceedings from the Solid Freeform Fabrication Symposium, Austin, pp 708–717

21. H. Wong, D. Neary, E. Jones, P. Fox, C. Sutcliffe (2018) Pilot capability evaluation of a feedback electronic imaging system prototype for in-process monitoring in electron beam additive manufacturing, Springer International Journal of Advanced Maufacturing Technology, in-press, DOI: 10.1007/s00170-018-2702-6

22. H. Wong, D. Neary, S. Shahzad, E. Jones, P. Fox, C. Sutcliffe (2018) Pilot Investigation of Feedback Electronic Image Generation in Electron Beam Melting and its Potential for In-Process Monitoring, Elsevier Journal of Materials Processing Technology, in-press, DOI: 10.1016/j.jmatprotec.2018.10.016

23. A. Dinh (2005) Noise and Noise Reduction Techniques, EE 323.3 Electronic Instrumentation teaching materials, College of Engineering, University of Saskatchewan, Canada

24. B. Dutta, F.H. Froes (2017) The Additive Manufacturing (AM) of titanium alloys, Metal Powder Report, Volume 72, Issue 2, pp. 96-106, ISSN 0026-0657, https://doi.org/10.1016/j.mprp.2016.12.062

25. M.J. Donachie (1988) Titanium; A Technical Guide. ASM International, pp. 31

26. A. Kirchner,B. Klöden, L. Luft, T. Weißgärber, B. Kieback (2014) Process Window for Electron Beam Melting of Ti-6Al-4V, Proceeding of EuroPM 2014 – AM Technologies

27. H. Bruining (1954) Physics and Applications of Secondary Electron Emission. London Pergamon Press Ltd, pp. 88

28. L. Reimer (1998) Scanning Electron Microscopy: Physics of Image Formation and Microanalysis, Springer, pp. 4 – 5

29. Arcam A1 EBM Machine Specification, Arcam AB

30. J.I. Goldstein, D.E. Newbury, J.R. Michael, N.W.M. Ritchie, J.H.J Scott, D.C. Joy (2018) Scanning Electron Microscopy and X-Ray Microanalysis (Forth Edition). Springer, pp. 30

31. G. Recktenwald (2010) Conversion of Thermocouple Voltage to Temperature, ME 449/549 teaching materials, Mechanical and Materials Engineering Department, Portland State Univeristy, USA

32. R.C. Gonzalez, R.E. Woods (2008) Digital Image Processing, Pearson Eductaion, Inc., pp. 122-127, 322-327

33. M. Reiter, D. Weiss, D, C. Gusenbauer, M. Erler, C. Kuhn, S. Kasperl, J. Kastner (2014) Evaluation of a Histogram-Based Image Quality Measure for X-ray Computed Tomography, Proceedsing of Conference on Industrial Computed Tomography 2014

34. N. Otsu (1979) A Threshold Selection Method from Gray-Level Histograms, IEEE Transactions on Systems, Man, and Cybernetics, Vol. SMC-9, No.1

35. T.A. Çengel, M.A. Boles (2011) Thermodynamics (Seventh Edition). McGraw Hill, pp. 93

36. B. Wysocki, P. Maj, R. Sitek, J. Buhagiar, K.J. Kurzydłowski, W. Święszkowski (2017) Laser and Electron Beam Additive Manufacturing Methods of Fabricating Titanium Bone Implants. Applied Sciences. 2017; 7(7): 657. https://doi.org/10.3390/app7070657

37. P.K. Jain, L.K. Sharma (1998) The Physics of blackbody radiation: A review, Journal of Applied Science in Southern Africa 4(2):80-101, DOI: 10.4314/jassa.v4i2.16899